Caving 2026 – A van As, D Cumming-Potvin & J Wesseloo (eds)

doi:10.36487/ACG_repo/2645_64

The utility of passive seismic attenuation tomography for monitoring changes in a block caving mine

Alejandro Jaimes [a,*], **Denver Julian Birch** [a]

[a] *Department of Applied Seismology, Institute of Mine Seismology, Australia*

Abstract

Travel-time tomography is a powerful non-invasive imaging technique that uses the first arrival travel times of P-waves (t_p) and S-waves (t_s) to infer the velocity of the medium through which seismic waves travel. This methodology has been successfully applied at block caving mines to map spatial and temporal variations in seismic velocities, which are then correlated to changes in the stress state of the rock mass. Much of this success can be attributed to the fact that, in general, seismic travel times, as well as ray paths, are significantly perturbed by the presence of the block cave. Despite their usefulness, velocity tomograms may not properly quantify areas of strong stress fracturing since variations in lithological properties can have a similar effect on the propagation time of seismic waves. Seismic quality factor (Q^{-1}) maps reflect the attenuation of seismic energy, which is highly sensitive to the extent of fracturing and crack accumulation. At block cave mines one is interested in tracking high stress areas. It is therefore beneficial to compute both 3D velocity and Q^{-1} maps.

In this work, we showcase a passive seismic attenuation tomography workflow to image both the velocity and attenuation structure through which seismic waves propagate. We first validate our framework with synthetic tests that use realistic source-to-receiver configurations, as well as physically meaningful velocity and attenuation models computed empirically from numerical stress models. We then use this methodology to obtain velocity and attenuation tomograms from passive seismic data recorded at an Australian block caving mine. These seismic data span a 12-month period and contain records from geophones and distributed acoustic sensing. The velocity and attenuation maps that were obtained are in agreement with previously estimated yielded zones. The attenuation maps, in particular, clearly delineate the progression of the yielded zone. The methodology that we present, and the associated results, highlight the potential of attenuation tomography to image high stress areas around block caving mines, which is of importance for geotechnical analyses.

Keywords: *seismicity, caving, seismic tomography, seismic attenuation*

1 Introduction

Spatial and temporal monitoring of caving, and the related phenomena, is necessary for successfully operating block caving mines. Because of its importance, cave propagation is monitored using devices such as optical and metallic time-domain reflectometers, tiltmeters and beacons. These devices produce pointwise measurements, which are used to subjectively interpolate the 3D cave shape (Kamp et al. 2022). Although these devices have become popular and their usage has become common practice in large-scale block caving operations, they fail to accurately monitor the complex 3D nature of caving processes (Hudyma et al. 2008). Over the last few decades, seismic monitoring has become an increasingly powerful complementary tool to assess cave propagation. Unlike previously mentioned geotechnical monitoring technologies, seismic monitoring is not confined to point measurements (Glazer & Hepworth 2005) because of the nature of seismic sources and seismic waves. Typically, caving-related seismic monitoring is limited to analysing the location of seismic events, seismic event rate, S-P energy ratio, size of seismic events, apparent stress and corner frequency, to name a few, with the goal of understanding the evolution of the seismogenic

* Corresponding author. Email address: alejandro.jaimes@imsi.org

zone surrounding block cave mines (Abolfazlzadeh & Hudyma 2016). Even though such analyses have significantly improved our understanding of cave propagation, they are limited to variations in the location of seismic events and their source properties, while ignoring meaningful waveform information such as the travel times or attenuation of seismic waves.

Travel-time tomography has gradually become an important technique for monitoring cave propagation. This technique uses the recorded travel times of first-arriving seismic waves to retrieve the velocity structure of the medium through which these waves travel. Because seismicity can occur at different sections of the cave and its surroundings, travel-time tomography can help quantify how the seismic velocities around the cave change over time by providing 3D maps of velocity variations. Changes in velocity are then empirically correlated to changes in stress by assuming that high stress areas have the effect of closing microcracks, resulting in an increase in seismic velocities (Baig et al. 2017). Remarkable applications of this technique include Westman et al. (2012) who used travel-time tomography to image a block cave mine over an 18-month period; Mercier et al. (2015) who used time-lapse travel-time tomography of block caves to understand how stresses are distributed and redistributed as well as the rock mass behaviour during development and production phases; and Hidayat et al. (2024) who performed 4D time-lapse tomography for monitoring cave propagation and stress redistribution. Much of the success of travel-time tomography in spatio-temporal monitoring of block caving operations can be attributed to the fact that the travel times and paths of seismic waves are strongly perturbed by the presence of the block caves that have material properties differing significantly from the surrounding background medium. Despite its success, velocity tomograms produced with travel-time tomography may not properly quantify areas of strong stress fracturing since variations in lithological properties can have a similar effect on the propagation time of seismic waves. Seismic quality factor (Q^{-1}) maps, computed via a method known as attenuation tomography, reflect the 3D attenuation of the energy of seismic waves, which is highly sensitive to the extent of fracturing and the development and accumulation of cracks. At block cave mines one is interested in tracking high stress areas and Q^{-1} maps can therefore be complementary to velocity maps. While seismic tomography in block cave mines has been mostly limited to travel-time tomography, attenuation tomography has been well developed in the seismology community. Some remarkable examples of this technique include determination of the attenuation structure in volcanic calderas (Clawson et al. 1989), quantification of regional variation of Q^{-1} at Loma Prieta, California, following an mW 6.9 main shock (Lees & Lindley 1994), and estimation of the extent of attenuation in the subduction zone beneath northern New Zealand (Wang et al. 2025), to name a few. We note that there have been some studies at mines, such as the study by Watanabe & Sassa (1996) who perform attenuation tomography for in situ rock testing at the Kamioka mine in Japan. Nevertheless, these studies have been limited as they assume a prior velocity model, meaning that errors in the output of travel-time tomography translate to errors in the output of attenuation tomography.

In this paper, we showcase a joint velocity-attenuation seismic tomographic inversion methodology, which we apply to seismic data, composed of both genuine events and blasts recorded at an Australian block caving mine. The tomography is performed using physics-informed neural networks (PINNs) based on an extension of the work by Jaimes et al. (2025a). The PINNs are solved by minimising an objective function that quantifies errors in recorded travel times (t) and attenuated times (t^*, characterising the spectral rate of decay of seismic waves), as well as errors in the respective physical laws. Thus, the inversion is physically consistent while respecting the recorded data. In Section 2, we provide a short discussion of the standard caving model of Duplancic & Brady (1999) and an alternative model based on damage zones around excavations as discussed by Perras & Diederichs (2016). In Section 3, we describe the methodology that we use to retrieve the input data t and t^*, as well as the inversion methodology that we develop and implement. In Section 4, we present results of application of the method to 12 months of synthetic and real seismic data split into quarterly steps. Synthetic models are computed by performing an ad hoc transformation from stress to velocity and attenuation models. These models are used to generate synthetic data t and t^*, which are then subsequently input to the inversion procedure to evaluate how accurately the original synthetic models are recovered. We conclude the paper in Section 5.

2 Caving models

Here, we provide an overview of 3 different caving models following the summary made by Jaimes et al. (2025b). The first model corresponds to that of Duplancic & Brady (1999), which has been widely adopted in hard rock mines worldwide. This model assumes that the volume containing the cave can be divided into 5 different regions:

- a caved zone filled with caved material able to rotate
- an airgap
- a zone of loosening, typically labelled the yield zone (YDZ), which covers regions that have degraded to zero cohesion or tensile strength
- a seismogenic zone, where seismic events occur due to discontinuous damage and the initiation of new fractures
- a surrounding pseudo-continuous domain of undisturbed rock mass.

Figure 1a illustrates the model developed by Duplancic & Brady (1999).

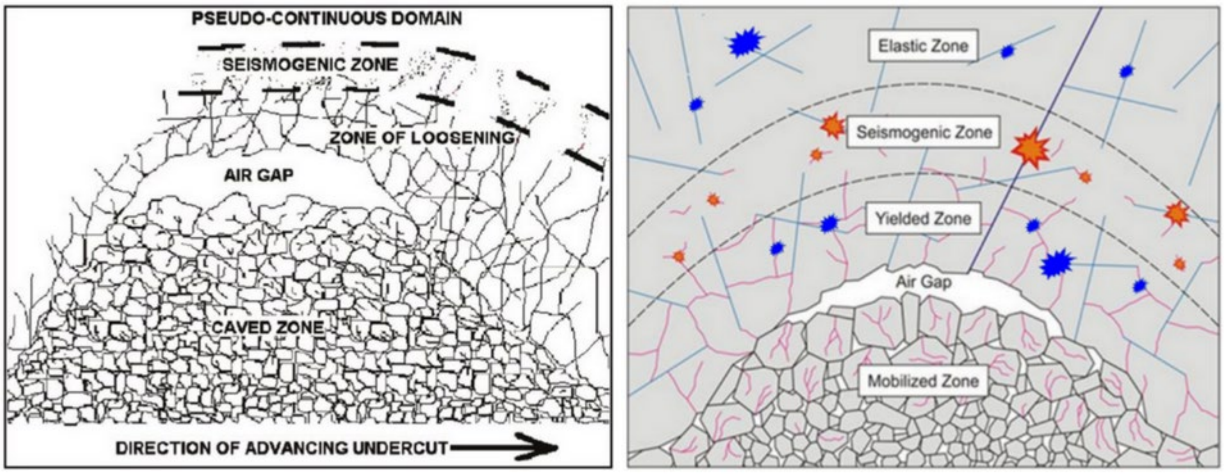

(a) (b)

Figure 1 (a) Conceptual model of caving from Duplancic & Brady (1999); (b) Modified version that is representative of the seismic response at block caving operations based on the work by Birch et al. (2022), where the blue symbols denote additional seismic events

A particular feature of this model is that seismic activity is assumed to only occur within the seismogenic zone. However, this feature is not in agreement with seismological observations at several caving operations (Birch et al. 2022). Birch et al. (2022) therefore proposed an alternative version of the earlier model (see Figure 1b) based on work by Sainsbury (2012). In this new model, seismic events are assumed to also occur outside the seismogenic zone, in yielded or elastic zones. At block caving operations it is of interest to monitor changes in the external boundary of the YDZ to verify that the cave is developing as expected and to minimise contamination of the cave by the host material. Furthermore, as caving progresses, it is fundamental to understand how the stresses are redistributed around the cave and the occurrence of damaging seismic events (Brown & Hudyma 2018), as well as how the cave grows to manage other geotechnical hazards that are not directly related to stress changes (Flores-Gonzales 2019). Recently, Perras & Diederichs (2016) described the various zones of damage that exist and develop around mining excavations. This model may be extended to caving by analysing the mechanics of damage around tunnels (Birch et al. 2022). Figure 2 shows an illustration of the zones of damage in this model.

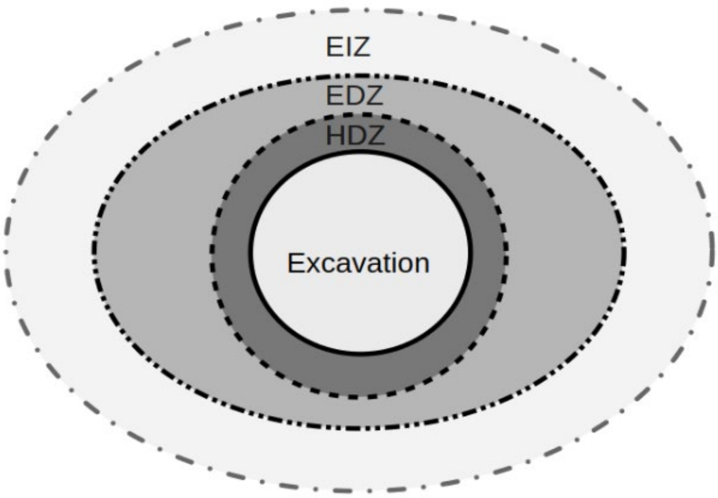

Figure 2 Conceptual models of caving and excavation damage zones highly damaged zone (HDZ), excavation damage zone (EDZ) and elastic influence zones (EIZ)

Table 1 shows the conceptual models as defined by Duplancic & Brady (1999), Salisbury (2012) and Perras & Diederichs (2016), where there is not necessarily a one-to-one correspondence between each of the zones in the models by Sainsbury (2012) and Perras & Diederichs (2016).

Table 1 Different conceptual models of caving and excavation damage zones

Duplancic & Brady (1999)	Sainsbury (2012)	Perras & Diederichs (2016)
Caved zone	Mobilised zone	Excavation
Airgap	Airgap	Highly damaged zone
Zone of loosening	Yield zone	Inner excavation damage zone
Seismogenic zone	Seismogenic zone	Outer excavation damage zone
Pseudo-continuous domain	Elastic zone	Elastic influence zone

The HDZ represents significantly fractured material around the excavation. This zone is surrounded by the total EDZ, both of which make up the YDZ. The EDZ is usually divided into an inner (EDZ_i) and outer (EDZ_o) zone. The boundary between these 2 sub-zones is quantitatively defined as the transition from volumetric expansion to contraction. In this paper, we assume that the combined HDZ and EDZ_i are equivalent to the zone of loosening defined in the model of Duplancic & Brady (1999). Lastly, there is an EIZ due to the presence of the excavation and its surrounding YDZ.

3 Methodology

In this section we describe travel-time and attenuation tomography, and the inversion framework that we develop.

3.1 Travel-time tomography

Travel-time tomography is a non-invasive imaging technique that uses the first-arrival travel times of seismic waves to retrieve the 3D velocity structure of the medium through which these waves travel.

In general, the relationship between the travel time and the velocity structure can be expressed as:

$$t(\mathbf{x}_s, \mathbf{x}_r) = \int_{L(\mathbf{x})} s(\mathbf{x}) dl \tag{1}$$

where

x_s	=	source location
x_r	=	receiver location
t	=	travel time from the source to the receiver location.

The integration path is denoted by the ray L(x), corresponding to the ray path with the shortest travel time from the source-to-receiver locations and s denotes slowness (i.e. inverse of velocity). Note that the integral in Equation 1 is hard to solve as the ray path itself depends on the unknown slowness model, thus requiring expensive raytracing computations. To address these complications, it is customary to instead compute travel times by solving the eikonal equation using finite differences (Vidale 1990):

$$|\nabla_{\mathbf{x}} t(\mathbf{x}_s, \mathbf{x})| = s(\mathbf{x}), \quad t(\mathbf{x}_s, \mathbf{x}_s) = 0 \tag{2}$$

with nabla representing the gradient operator with respect to the x coordinates. Note that, by definition, the travel time at the source is defined to be zero, and that Equation 2 follows from the wave equation in the high-frequency regime (Kim 2001). The classical approach to eikonal-based travel time tomography (Watanabe et al. 1999; Tresiter & Haber 2016; Liu & Tong 2021) consists of repeatedly solving Equation 2 with the goal of finding the slowness model that produces synthetic travel times that most closely match the measured travel times.

3.2 Attenuation tomography

Similar to travel-time tomography, attenuation tomography is a non-invasive imaging technique that aims to map the structure of the medium through which seismic waves travel. However, with this method one aims to infer the attenuative properties of the propagating medium. A significant benefit of this technique is that the attenuation of seismic amplitudes/energies is highly sensitive to the extent of fracturing and crack accumulation and the quantification of attenuation can therefore be complementary to velocity tomograms. In fact, assuming a Brune source model (Brune 1970), one may represent the displacement spectrum of a seismic event recorded at a given receiver as:

$$H(f) = \frac{\Omega_0 \exp[-\pi f t^*]}{1 + (f/f_c)^2} \tag{3}$$

where

f	=	frequency
Ω_0	=	low-frequency plateau, which is directly proportional to the seismic potency
f_c	=	corner frequency
t^*	=	a parameter that quantifies the extent of attenuation (Q^{-1}) along the ray path and is typically referred to as the attenuated time.

For a given ray path, velocity and frequency, higher t^* corresponds to higher attenuation. The relationship between t^* and the seismic quality factor Q is given by:

$$t^*(\mathbf{x}_s, \mathbf{x}_r) = \int_{L(\mathbf{x})} Q^{-1}(\mathbf{x}) s(\mathbf{x}) dl \tag{4}$$

where L(x) is defined the same way as in Equation 1 assuming that attenuation is small enough and Q^{-1} is defined as the inverse of the seismic quality factor Q. If one assumes that attenuation is uniform then it follows that $t^* = Q^{-1}t$. Note that while the parameter Q has been empirically correlated with the well-known rock mass quality factor, they correspond to different quantities. In general, low Q values correspond to extensively fractured material, thus high attenuation, while high Q values correspond to a compact and competent rock mass, thus low attenuation. The typical approach in attenuation tomography is to first estimate a velocity model with travel-time tomography and then use this model in Equation 4 to find the 3D Q structure that produces the synthetic t^* that best matches the attenuated times measured from the decay of the displacement spectrum (Lees & Lindley 1994). In this way, the ray path required to solve Equation 4 is already known from travel-time tomography. While this hierarchical approach has found much use in seismological applications, it may be limited as errors in the velocity may degrade the quality of attenuation inversions. It is therefore beneficial to combine velocity and attenuation tomography into a single workflow to maximise the advantage of the robustness of velocity with the sensitivity to the micro-structure of attenuation (Debski & Young 1999).

3.3 Joint velocity-attenuation inversion

Classical attenuation tomography requires a velocity model in advance so that raytracing can be performed (Guo & Thurber 2021), which limits its performance and may introduce unwanted trade-offs. This requirement can be circumvented by making use of the fact that one can treat wave propagation in a viscoelastic (or viscoacoustic) medium as wave propagation through an elastic (or acoustic) medium with complex-valued parameters (or a complex-valued velocity). Recently, Hu et al. (2021) showed that, in the presence of attenuation characterised by the seismic quality factor Q, an advection equation (analogous to Equation 2) arises for the attenuated time t^*:

$$\nabla_{\mathbf{x}} t(\mathbf{x}_s, \mathbf{x}) \cdot \nabla_{\mathbf{x}} t^*(\mathbf{x}_s, \mathbf{x}) = Q^{-1}(\mathbf{x}) s^2(\mathbf{x}), \quad t^*(\mathbf{x}_s, \mathbf{x}_s) = 0 \tag{5}$$

where the attenuated time is defined as zero at the source. By jointly solving Equations 2 and 5, subject to measured travel (t) and attenuated (t^*) times, one may determine the slowness and attenuation models producing synthetic data that most closely match the recorded data.

3.4 Inversion framework

3.4.1 Physics-informed neural networks

The inversion framework that we developed to jointly invert for velocity and attenuation is based on PINNs, following the work of Jaimes et al. (2025a) who formulated PINNs for travel-time tomography. PINNs are a natural tool for tomographic problems as the neural network can be used to learn the forward model (i.e. the solution to the eikonal and advection equations, Equations 2 and 5, respectively) and the inverse problem (i.e. retrieving the parameters of interest) simultaneously in the learning process, which is advantageous for dealing with large-scale 3D settings as in block caving operations. PINNs are a type of artificial neural networks (ANNs) the outputs of which are constrained by physical laws (Raissi et al. 2019). They consist of a collection of neurons or nodes, which are connected through a sequence of layers. While there are many types of ANNs (Schmidhuber 2015), in this paper we focus on residual forward feed neural networks. By construction, these networks only have connections in the forward direction, starting with an input layer containing a set of nodes, denoted as features (spatial coordinates in the context of this work), traversing through interconnected layers of neurons, denoted as hidden layers, and concluding with an output layer containing the desired output $\mathcal{U}(\cdot)$. Denoting y_k^l as the k^{th} node in layer l, one can recursively define the output at the node y_k^{l+1} as:

$$y_k^{l+1} = \sigma_l \left(\sum_{m=1}^{N_l} W_{km}^{l+1} y_m^l + b_k^{l+1} \right) + y_k^l \tag{6}$$

where N_l is the number of nodes in layer l, W_{km}^{l+1} is the weight of the connection between nodes y_m^l and y_k^{l+1}, b_k^{l+1} is the bias at node y_k^{l+1} and σ_l is the element-wise non-linear activation function at layer l+1. Many non-linear activation functions have been proposed in the past for various machine-learning applications (Jagtap & Karniadakis 2023). In this paper we use the hyperbolic tangent function, tanh. Via a cascade of operations one uses the update in Equation 6 to recursively propagate the features through the neural network. The weights and biases are referred to as the tunable weights, $\boldsymbol{\theta} = \{\mathbf{W},\mathbf{b}\}$. The goal with ANNs is then to find the optimal weights $\boldsymbol{\theta}^*$ that minimise a given objective function. In the context of PINNs-based tomography, the optimal weights are those which provide the best fit to both the conservation laws (eikonal and advection equations) and the data (t and t^*) residuals.

3.4.2 PINNs-based tomography

Since the foundational work of Raissi et al. (2019), PINNs have emerged as a powerful and convenient tool for solving forward and inverse problems involving non-linear partial differential equations, such as the eikonal and advection equations described in this paper. In the context of tomography, we aim to use the eikonal equation (Equation 2) and advection equation (Equation 5) to determine the slowness $s(\mathbf{x})$ and the seismic quality factor $Q(\mathbf{x})$ which most closely explain the measured data t and t^*. Here, we provide a summary of the PINNs-based tomography. For the intricacies of the PINNs formulation we refer the reader to Jaimes et al. (2025a). The goal with PINNs-based tomography is to find neural networks $\mathcal{N}_t$, $\mathcal{N}_{t^*}$, $\mathcal{N}_s$ and $\mathcal{N}_Q$, which most closely satisfy the eikonal and advection equations, subject to $\mathcal{N}_t$ and $\mathcal{N}_{t^*}$ matching the recorded data t and t^* at a set of sources and receivers. We thus construct the following objective function, which we seek to minimise :

$$
\begin{aligned}
J(\theta) \quad &= \mathbb{E}_{\mathbf{x}'\sim\rho_s}\mathbb{E}_{\mathbf{x}\sim\rho}\left[\left(\mathcal{L}^{\text{eik}}(\mathbf{x}',\mathbf{x};\theta_t) - f^{\text{eik}}(\mathbf{x};\theta_s)\right)^2 + \left(\mathcal{L}^{\text{adv}}(\mathbf{x}',\mathbf{x};\theta_t,\theta_{t^*}) - f^{\text{adv}}(\mathbf{x};\theta_s,\theta_Q)\right)^2\right] \\
&+ \frac{1}{N_s N_r}\sum_{i=1}^{i=N_r}\sum_{j=1}^{j=N_s}\left[\left(t^{\text{pred}}(\mathbf{x}_j,\mathbf{x}_i;\theta_t) - t^{\text{data}}(\mathbf{x}_j,\mathbf{x}_i)\right)^2 + \left(t^{*\text{pred}}(\mathbf{x}_j,\mathbf{x}_i;\theta_{t^*}) - t^{*\text{data}}(\mathbf{x}_j,\mathbf{x}_i)\right)^2\right]
\end{aligned}
\tag{7}
$$

where:

i and j	=	integers that denote the receiver and source indices, respectively
$\mathcal{L}^{\text{eik}}$ and f^{eik}	=	left-hand-side and right-hand-side terms of the eikonal equation, respectively
$\mathcal{L}^{\text{adv}}$ and f^{adv}	=	left-hand-side and right-hand-side terms of the advection equation, respectively
$E_{\mathbf{x}'}$ and $E_{\mathbf{x}}$	=	sampling expectation of virtual source and receiver coordinates, respectively, over which the physical residuals in Equation 7 are evaluated
$\boldsymbol{\theta} = (\boldsymbol{\theta}_t, \boldsymbol{\theta}_{t^*}, \boldsymbol{\theta}_s, \boldsymbol{\theta}_Q)$	=	parameter that denotes the set of weights for the travel and attenuated times, slowness and seismic attenuation, respectively, that we aim to optimise .

Specifically, we want to find the optimal weights that minimise the physical and data residuals in Equation 7:

$$
\theta^{\text{opt}} = \text{argmin}_{\theta\in\Theta} J(\theta) \tag{8}
$$

To minimise the objective function, we use the Adaptive Moment Estimation (ADAM) algorithm, a widely used and efficient method for stochastic optimisation (Kingma & Ba 2014). After the optimisation has concluded, the best slowness and inverse attenuation models are determined by evaluating the corresponding networks at the optimal weights. Note that this tomographic algorithm is gridless; the inversion outputs are instead functions that map the input features (i.e. spatial coordinates) to a velocity/attenuation model.

4 Application to a block caving operation

4.1 Seismic dataset

The seismic data that we use for the tomographic inversions consist of 12 months of records obtained at an Australian block caving mine. The dataset contains genuine events as well as production blasts. The production blasts were incorporated as they happen to increase the ray coverage. Quarterly periods, denoted as Q1, Q2, Q3 and Q4 are considered. Table 2 shows a summary of the datasets that were used and Figure 3 shows their spatial distribution for the different timesteps. Notice that most of the seismicity is limited to the eastern section of the domain. Furthermore, over time the seismicity migrates upwards and to the east, thus, we would expect the yielded zone to also migrate toward the same direction. In the same manner, we would expect that any evolution in the spatial extent of the yielded zone is reflected in the attenuation and velocity models that we invert.

Table 2 Summary of datasets used in the inversion

Step	Number of seismic events	Number of t and t^* measurements
Q1	5,200	45,997
Q2	5,777	52,840
Q3	6,393	60,276
Q4	6,807	59,922

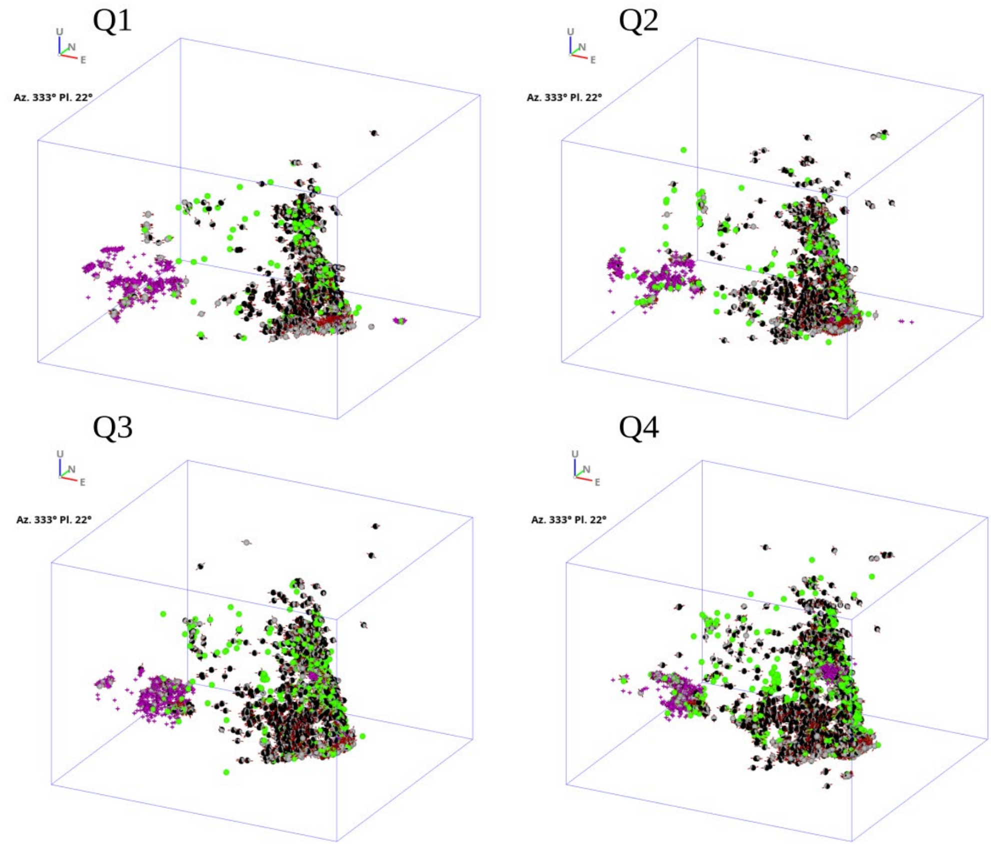

Figure 3 Seismic datasets used for the tomographic inversions divided by quarter. Blasts are denoted by purple stars, genuine events with mechanisms are denoted by beachballs and genuine events without mechanisms are denoted by green spheres. The blue outline indicates the inversion domain

4.2 Verification of inversion with synthetic data

To validate the inversion methodology developed in this paper, as well as to assess the reliability of the application of the method to field data, we construct synthetic velocity and attenuation models following the approach by Jaimes et al. (2025b). These models are used to generate forward-modelled data t and t^*, which are then used as input data in the inversion, with the goal of assessing how well the original models are retrieved. Note that these models should not be constructed in an arbitrary manner and should rather represent, to some extent, the geometry of caving processes. We therefore solve for the maximum principal stress, σ_1, using the Material Point Method (MPM; Nairn 2003). The material properties and in situ stress used for modelling are the same as that of Jaimes et al. (2025b).

The obtained stress model is converted to a velocity model by applying the following piecewise transformation by Jaimes et al*.* (2025b):

$$v(x) := \begin{cases} v_1 + (v_2 - v_1) \cdot \dfrac{\sigma_1(x)}{C}, & \sigma_1(x) < C \\ v_2 + (v_3 - v_2) \cdot \dfrac{\sigma_1(x) - C}{\max(\sigma_1(x)) - C}, & C \leq \sigma_1(x) \leq \max(\sigma_1(x)) \end{cases} \tag{8}$$

where C and max(σ_1) are arbitrary constants that are set to 100 and 140 MPa. The earlier describes the magnitude at which the linear relationship between stresses and velocities change, while the latter is the maximum compressive stress. The values of v_1, v_2 and v_3 are set to 5, 6.5 and 7 km/s, respectively. In this transformation, we assign high velocities to areas of high stress and low velocities to areas of low stress. The transformation from stresses to velocities is done to obtain realistic reference models that can be used in the synthetic tests. A similar transformation is applied to the velocity model to construct an attenuation model. Figure 4 shows oblique and plan views of the synthetic velocity and attenuation models. Inside the cave, denoted by the sharp contrast, low velocity and attenuation is assigned, corresponding to highly fractured material. On the cave footprint, high velocities and attenuation values are assigned, corresponding to increased stresses.

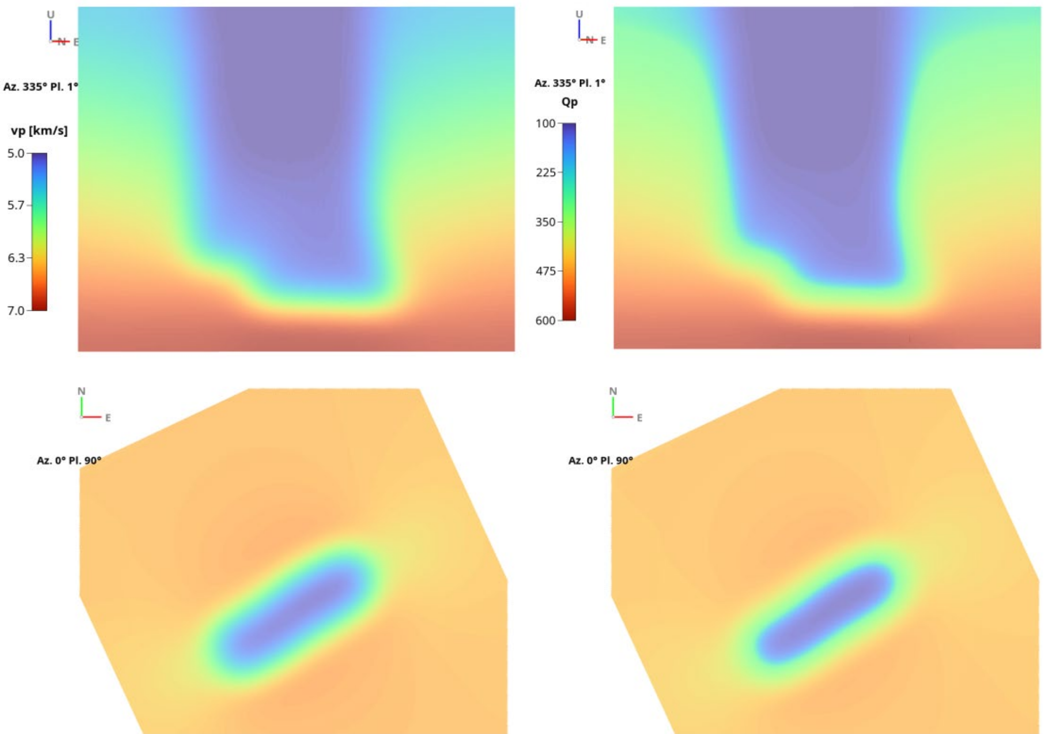

(a) (b)

Figure 4 Oblique (top) and plan (bottom) view of the (a) synthetic velocity and (b) attenuation models

Here, for illustration purposes, we consider only the results (velocity model) from the inversion of the synthetic data corresponding to Q1. The corresponding velocity models (first row), as well as the errors with the true models (second row), are shown in Figure 5 for the same views as Figure 4. Overall, there is a good agreement – in terms of retrieved velocity values (<5% error) – between the inverted and original models. The locations with the most significant errors situate in the western section of the cave where seismic coverage is poor and the model is poorly constrained (see Figure 3). There are other regions with significant error towards the middle and upper sections of the cave, as a result of a limited number of ray paths intersecting these regions due to ray bending around the cave boundary as a result of the low velocity zone. The bottom row shows areas of the inverted model that are within 0.3 km/s of the true values. Regions exceeding this threshold are denoted as uncertain and will be filtered out from the results shown in the next section.

4.3 Application to seismic data from a block caving operation

The joint velocity-attenuation inversion methodology that we developed was applied at an Australian block caving operation. We run the inversion for 4,000 epochs and to display the resulting models we use a grid spacing of 25 m. Note, however, that the inversion algorithm is gridless and thus a smaller spacing may be used without any added computational costs. Figures 6 and 7 show the inverted velocity and attenuation models, respectively, along the same cross-sections as Figure 5. A historical cave shape is displayed as a grey contour and yielded zones previously constructed are shown as purple thin strips. At this operation, the mine conducts quarterly surveys of the yielded zone shape based on recorded seismic data. A variety of inputs, each with their own geomechanical relationship to yielding rock mass, are extracted from the results of routine seismic data processing and combined in a repeatable manner to systematically track the progression of the yielded zone. Typical inputs include, but are not limited to, estimates of event hypocentres and associated source parameters, seismic moment tensors and velocity maps estimated from body-wave travel-time tomography. The velocity maps shown in Figure 6 agree well with the hypothesised yielded zone progression. The area of low velocity migrates toward the east and also slightly upwards as the yielded zone extends. On the cave footprint, high velocities are observed. Similar features are observed in the attenuation maps shown in Figure 7. A low Q area, corresponding to high attenuation, is seen to migrate upwards slightly and to the east as the yielded zone moves in the same direction. In particular, the plan view of the attenuation maps clearly delineates a high attenuation area (dark blue), which follows the evolution of the yielded zone. This low Q area develops as the rock mass becomes fractured with the expansion of the yielded zone. Note that the low velocity and seismic quality factor observed in the eastern-upper region of the vertical cross-section is attributed to local geology.

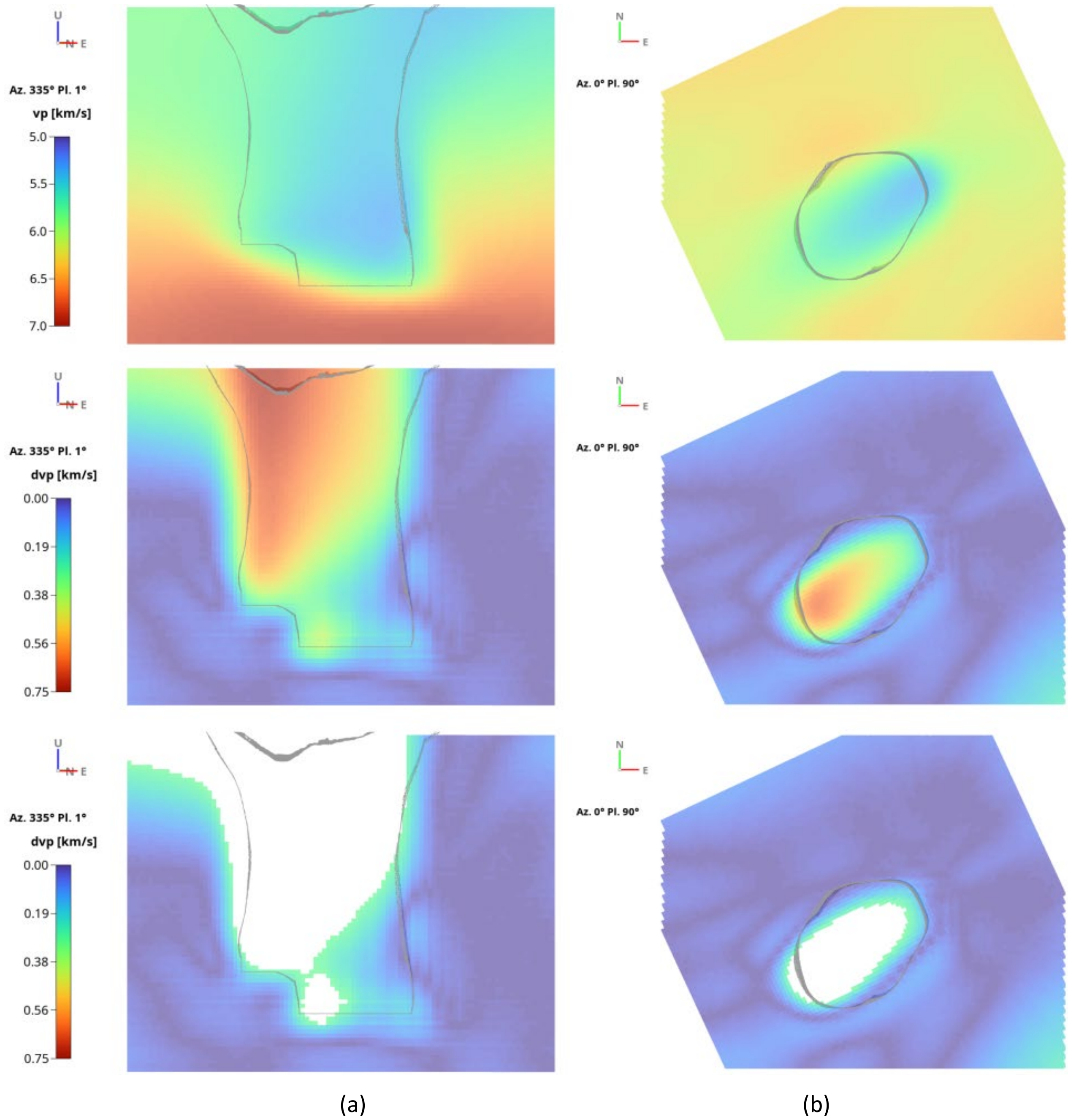

Figure 5 **(a) Oblique and (b) plan views of the inverted velocity (top) and difference with the true model (middle). The bottom row corresponds to the middle row after filtering out areas where the velocity error is greater than 0.3 km/s and the grey outline corresponds to a historical cave plus yielded zone shape**

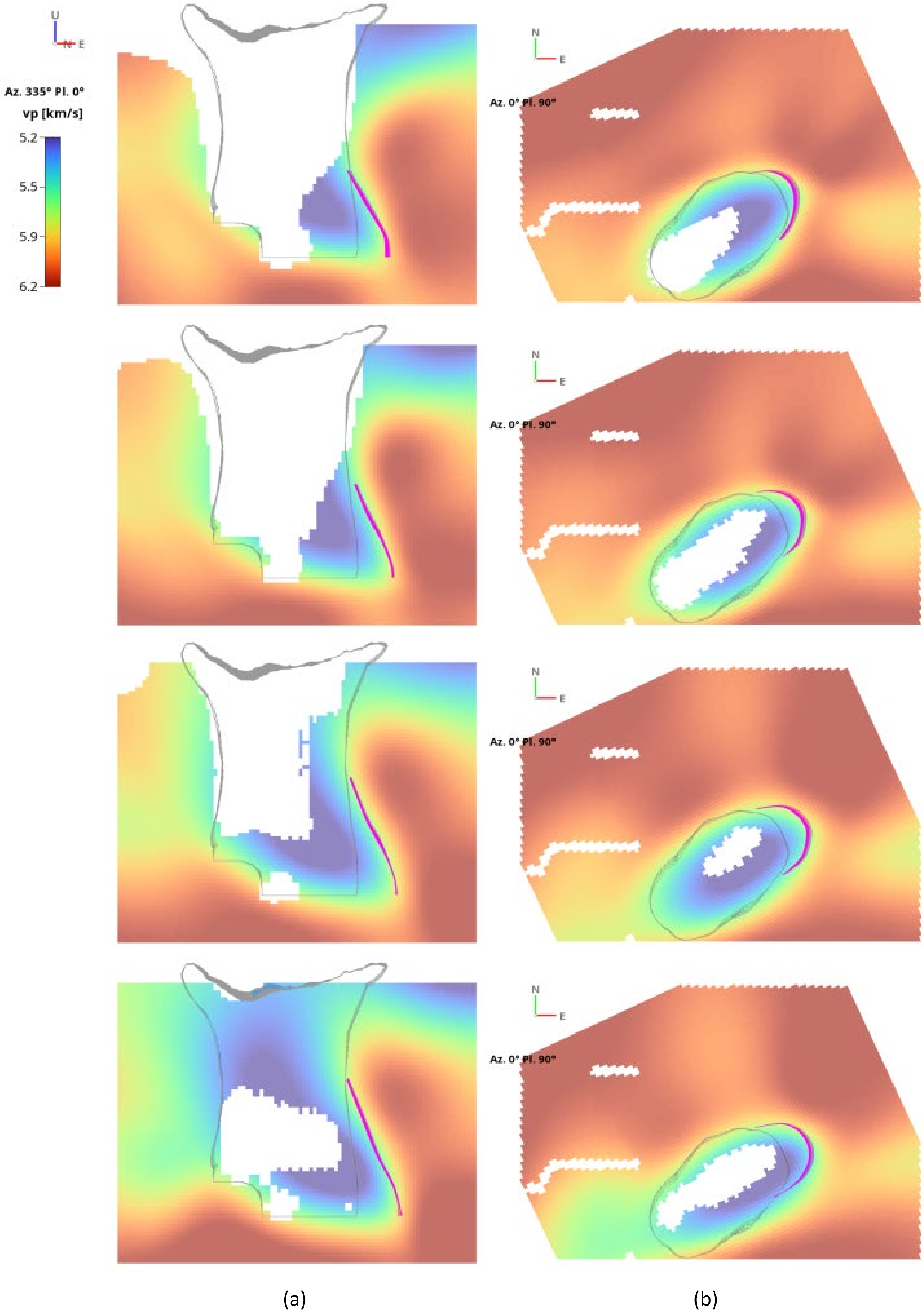

Figure 6 (a) Oblique and (b) plan view comparing the velocity models from Q1 (top) to Q4 (bottom)

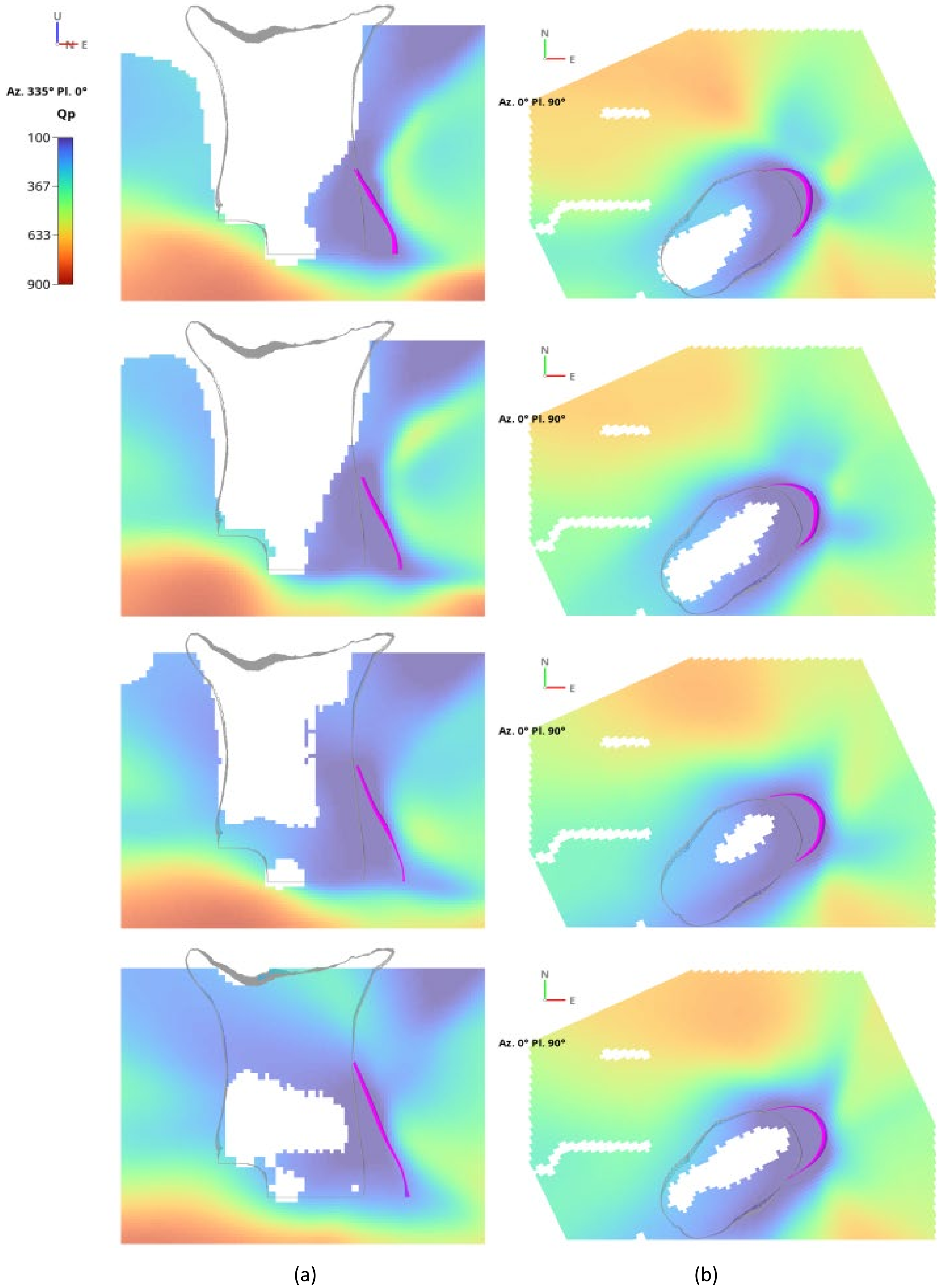

Figure 7 (a) Oblique and (b) plan view comparing the attenuation models from Q1 (top) to Q4 (bottom)

While seismic tomography at block caving mines is mostly limited to travel-time tomography, there is additional value in extending typical tomographic algorithms to also invert for the attenuative properties of the rock mass. Because the seismic quality factor reflects the attenuation of seismic amplitudes and energies, which is highly sensitive to the extent of fracturing and crack accumulation, it is beneficial to incorporate attenuation tomography into standard cave tracking methodologies.

5 Conclusion

Seismic tomographic algorithms used at block caving mines are usually limited to body-wave first-arrival travel-time tomography, which uses the arrival time of seismic waves to infer 3D seismic velocity maps of the rock mass through which the waves travel. These velocity tomograms, while useful, may fail to properly quantify areas of high stress fracturing as variations in lithological properties may similarly affect seismic travel times. Seismic attenuation maps, which quantify the spectral rate of decay of seismic amplitudes, have been used for decades in the seismology community to better characterise highly fractured regions and are complementary to velocity maps. This technique can be similarly used to monitor the evolution of a cave and its yielded zone as similar geomechanical features are expected. Much of the success of this technique is attributed to the fact that seismic attenuation is more sensitive to fractures than to seismic velocities. The main drawback of this technique is that a prior velocity model is assumed so that seismic rays can be traced through the inversion domain. In this paper, we propose a joint velocity-attenuation inversion workflow that uses seismic travel times as well as attenuated times to determine 3D velocity and attenuation maps of the rock mass through which seismic waves propagate. Our workflow is implemented using PINNs by constructing an objective function that measures errors in the recorded seismic data while maintaining fidelity to the underlying physics. This algorithm is first tested on a synthetic dataset, which is built using realistic velocity and attenuation models. The inverted models agree well with the original models in areas where coverage is sufficient, as shown in Figure 5. We applied this algorithm to seismic data spanning a 12-month period, divided in 4 equal time periods. The velocity and attenuation maps that were obtained agree well with previously estimated yielded zones. The attenuation maps, in particular, clearly delineate the progression of the yielded zone (see Figure 7). While not discussed in detail, attenuation tomography can also help improve estimates of source parameters, such as seismic energy, since some of these parameters are highly dependent on the unknown spectral rate of decay of seismic waves. The work shown in this paper highlights the potential for using attenuation tomography to image high stress areas around block caving mines. Such imaging is of importance for geotechnical analyses and can potentially improve the robustness of cave yielded zone tracking methodologies.

6 Acknowledgement

We thank colleagues at the Institute of Mine Seismology for fruitful discussions, as well as the anonymous reviewers who helped improve this manuscript. The results presented in this paper are obtained in terms of the Research Project of the Institute of Mine Seismology ‘Tomographic Methods in Underground Mines’ supported by Codelco, Harmony, Sibanye-Stillwater, LKAB, Newcrest and PT Freeport Indonesia.

References

Abolfazlzadeh, Y & Hudyma, M 2016, ‘Identifying and describing a seismogenic zone in a sublevel caving mine’, *RockMechanics and Rock Engineering*, vol. 49, pp. 3735–3751, https://doi.org/10.1007/s00603-016-1017-x

Baig, AM, Bosman, K & Urbancic, TI 2017, ‘Temporal changes in stress state imaged through seismic tomography’, in J Wesseloo (ed.), *Deep Mining 2017: Proceedings of the Eighth International Conference on Deep and High Stress Mining*, Australian Centre for Geomechanics, Perth, pp. 269–273, https://doi.org/10.36487/ACG_rep/1704_18_Baig

Birch, D, Basson, G & Rigby, A 2022, *Temporal Changes in Stress State Imaged Through Seismic Tomography*, technical report, Institute of Mine Seismology

Brown, LG & Hudyma, MR 2018, ‘Identifying a migrating stress front using apparent stress for an unplanned rock mass cave’, in Y Potvin & J Jakubec (eds), *Caving 2018: Proceedings of the Fourth International Symposium on Block and Sublevel Caving*, Australian Centre for Geomechanics, Perth, pp. 565–576, https://doi.org/10.36487/ACG_rep/1815_44_Brown

Brune, JN 1970, 'Tectonic stress and the spectra of seismic shear waves from earthquakes', *Journal of Geophysical Research* , vol. 75, no. 26, pp. 4997–5009, https://doi.org/10.1029/JB075i026p04997

Clawson, S, Smith, R & Benz, H 1989, 'P wave attenuation of the Yellowstone Caldera from three-dimensional inversion of spectral decay using explosion source seismic data', *Journal of Geophysical Research: Solid Earth*, vol. 94, pp. 7205–7222, https://doi.org/10.1029/JB094iB06p07205

Debski, W & Young, RP 1999, 'Enhanced velocity tomography: Practical method of combining velocity and attenuation parameters', *Geophysical Research Letters*, vol. 26, no. 21, pp. 3253–3256, https://doi.org/10.1029/1998GL010368

Duplancic, P & Brady, BH 1999, 'Characterization of caving mechanisms by analysis of seismicity and rock stress', *Proceedings 9th International Congress on Rock Mechanics*, vol. 2, pp. 1049–1053.

Flores-Gonzalez, G 2019, 'Major hazards associated with cave mining: are they manageable?', in J Wesseloo (ed.), *MGR 2019: Proceedings of the First International Conference on Mining Geomechanical Risk*, Australian Centre for Geomechanics, Perth, pp. 31–46, https://doi.org/10.36487/ACG_rep/1905_0.3_Flores-Gonzalez

Glazer, SN & Hepworth, N 2005, 'Seismicity Induced by cave mining, Palabora experience', in Y Potvin & M Hudyma (eds), *RaSiM6: Proceedings of the Sixth International Symposium on Rockburst and Seismicity in Mines Proceedings*, Australian Centre for Geomechanics, Perth, pp. 281–289, https://doi.org/10.36487/ACG_repo/574_26

Guo, H & Thurber, C 2021, 'Double-difference seismic attenuation tomography and its application to The Geysers geothermal field, California', *Geophysical Journal International*, vol. 225, no. 2, pp. 926–949, https://doi.org/10.1093/gji/ggab017

Hidayat, W, Sahara, DP, Widiyantoro, S, Suharsono, S, Riyanto, E, Nukman, M, … Ambata Putra, IPR 2024, '4D time lapse tomography for monitoring cave propagation and stress distribution in deep mill level zone (DMLZ) PT Freeport Indonesia', *Geomechanics and Geophysics for Geo-Energy and Geo-Resources*, vol. 10, no. 39, https://doi.org/10.1007/s40948-023-00718-w

Hu, J, Qian, J, Song, J, Ouyang, M, Cao, J & Leung, S 2021, 'Eulerian partial-differential-equation methods for complex-valued eikonals in attenuating media', *Geophysics*, vol. 86, no. 4, pp. 179–192, https//doi.org/10.1190/geo2020-0659.1

Hudyma, M, Potvin, Y & Allisons, D 2008, 'Seismic monitoring of the Northparkes Lift 2 block cave - Part I undercutting', *Journal of the Southern African Institute of Mining and Metallurgy*, vol. 108, no. 7, pp. 405–419, https://www.saimm.co.za/Journal/v108n07p405.pdf

Jagtap, AD & Karniadakis, GE 2023, 'How important are activation functions in regression and classification? a survey, performance comparison, and future directions', *Journal of Machine Learning for Modelling and Computing*, vol. 4, no. 1, pp. 21–75, http//dx.doi.org/10.1615/JMachLearnModelComput.2023047367

Jaimes, MA, Rigby, A, Birch, D & Lotter, E 2025a, 'Noninvasive imaging of the underground via travel-time tomography: overview and recent developments', in S Dineva (ed.), *RaSiM11: Proceedings of the 11th International Symposium on Rockbursts and Seismicity in Mines*, Luleå University of Technology, Luleå, pp. 337–355.

Jaimes, MA, Malovichko, D, Lotter, E, Rigby, A & Birch, D 2025b, 'Target-oriented Imaging of the underground: tracking the growth of cave damage zones using seismic travel times', in S Dineva (ed.), *RaSiM11: Proceedings of the 11th International Symposium on Rockbursts and Seismicity in Mines*, Luleå University of Technology, Luleå, pp. 466–484.

Kamp, C, Conley, A, Collins, DS, Preiksaitis, M, Butler, T & Shumila, V 2022, 'Use of seismic tomography to aid rock mechanics interpretation at New Afton B3 block cave mine', in Y Potvin (ed.), *Caving 2022: Proceedings of the Fifth International Conference on Block and Sublevel Caving*, Australian Centre for Geomechanics, Perth, pp. 461–472, https://doi.org/10.36487/ACG_repo/2205_31

Kim, S 2001, 'The most energetic traveltime of seismic waves', *Applied Mathematics Letters*, vol. 14, no. 3, pp. 313–319, https://doi.org/10.1016/S0893-9659(00)00155-5

Kingma, D & Ba, J 2014, 'Adam: a method for stochastic optimization', *CoRR*, https://api.semanticscholar.org/CorpusID:6628106

Lees, J & Lindley, G 1994, 'Three-dimensional attenuation tomography at Loma Prieta: Inverting of t^* for Q', *Journal of Geophysical Research: Solid Earth* , vol. 99, pp. 6843–6863, https://doi.org/10.1029/93JB03460

Liu, Y & Tong, P 2021, 'Eikonal equation-based P-wave seismic azimuthal anisotropy tomography of the crustal structure beneath northern California', *Geophysical Journal International*, vol. 226, no. 1, pp. 287–301, http://https//doi.org/10.1093/gji/ggab103

Mercier, JP, de Beer, W, Mercier, JP & Morris, S 2015, 'Evolution of a block cave from time-lapse passive source body-wave traveltime tomography', *Geophysics*, vol. 80, no. 2, pp. 85–97, https://doi.org/10.1190/geo2014-0155.1

Nairn, JA 2003, 'Material point method calculations with explicit cracks', *Computer Modeling in Engineering and Sciences*, vol. 4, no. 6, pp. 649–664, https://doi.org/10.3970/cmes.2003.004.649

Perras, M, & Diederichs, M 2016, 'Predicting excavation damage zones in brittle rocks', *Journal of Rock Mechanics and Geotechnical Engineering*, vol. 8, no. 1, pp. 60–74, https://doi.org/10.1016/j.jrmge.2015.10.004

Raissi, M, Perdikaris, P & Karniadakis, GE 2019, 'Physics-informed neural networks: a deep learning framework for solving forward and inverse problems involving nonlinear partial differential equations', *Journal of Computational Physics*, vol. 378, pp. 686–707, https://doi.org/10.1016/j.jcp.2018.10.045

Sainsbury, B 2012, *A Model for Cave Propagation and Subsidence Assessment in Jointed Rock Masses*, PhD thesis, UNSW, Sydney.

Schmidhuber, J 2015, 'Deep learning in neural networks: an overview', *Neural Networks*, vol. 61, pp. 85–117, http//dx.doi.org/10.1016/j.neunet.2014.09.003

Treister, E & Haber, E 2016, 'A fast marching algorithm for the factored eikonal equation', *Journal of Computational Physics*, vol. 324, pp. 210–225, https://doi.org/10.1016/j.jcp.2016.08.012

Vidale, JE 1990, 'Finite-difference calculation of traveltimes in three dimensions', *Geophysics*, vol. 55, no. 5, pp. 521–526, http://https//doi.org/10.1190/1.1442863

Wang, D, Chen, J, Wu, S, Li, T, Bai, Y, Gao, Y & Tong, P 2025, 'Adjoint-State Attenuation Tomography: Method and Application to Northern New Zealand, *Journal of Geophysical Research: Solid Earth* , vol. 130, no. 11, https://doi.org/10.1029/2025JB031822

Watanabe, T & Sassa, K 1996, 'Seismic attenuation tomography and its application to rock mass evaluation', *International Journal of Rock Mechanics and Mining Sciences & Geomechanics Abstracts*, vol. 33, no. 5, pp. 467–477, https://doi.org/10.1016/0148-9062(96)00005-8

Watanabe, Y, Matsuoka, T & Ashida, Y 1999, 'Seismic traveltime tomography using Fresnel volume approach', *SEG Technical Program Expanded Abstracts*, pp. 1402–1405, https://doi.org/10.1190/1.1820777

Westman, E, Luxbacher, K & Schafrik, S 2012, 'Passive seismic tomography for three-dimensional time-lapse imaging of mining-induced rock mass changes', *The Leading Edge*, vol. 31, no. 3, pp. 338–345, https://doi.org/10.1190/1.3694902